

Motion Matters: Compact Gaussian Streaming for Free-Viewpoint Video Reconstruction

Jiacong Chen^{1,2} Qingyu Mao³ Youneng Bao⁴ Xiandong Meng⁵ Fanyang Meng⁵
Ronggang Wang^{5,6} Yongsheng Liang^{1,2}✉

¹College of Applied Technology, Shenzhen University, Shenzhen, China

²College of Big Data and Internet, Shenzhen Technology University, Shenzhen, China

³College of Electronics and Information Engineering, Shenzhen University, Shenzhen, China

⁴Department of Computer Science, City University of Hong Kong, Hong Kong, China

⁵Pengcheng Laboratory, Shenzhen, China

⁶School of Electronic and Computer Engineering, Peking University, Shenzhen, China

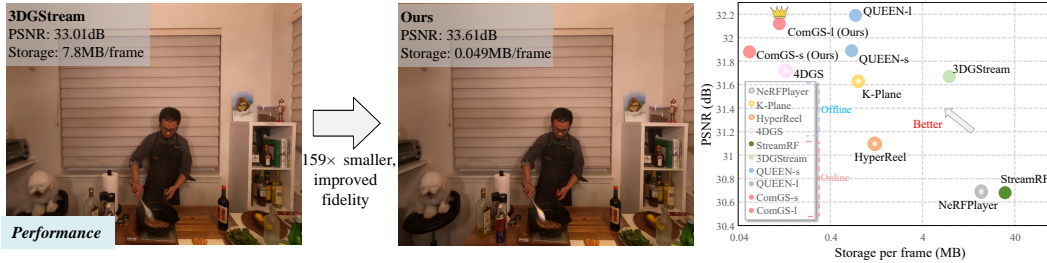


Figure 1: **Left:** Experimental results on N3DV dataset [14] showcase the effectiveness of our method, which reduces the storage requirement of 3DGSStream [13] by $159 \times$, with enhanced visual quality. **Right:** Comparison with existing methods in storage and reconstruction fidelity. Hollow circles denote offline methods, while solid circles represent online methods.

Abstract

3D Gaussian Splatting (3DGS) has emerged as a high-fidelity and efficient paradigm for online free-viewpoint video (FVV) reconstruction, offering viewers rapid responsiveness and immersive experiences. However, existing online methods face challenge in prohibitive storage requirements primarily due to point-wise modeling that fails to exploit the motion properties. To address this limitation, we propose a novel Compact Gaussian Streaming (ComGS) framework, leveraging the locality and consistency of motion in dynamic scene, that models object-consistent Gaussian point motion through keypoint-driven motion representation. By transmitting only the keypoint attributes, this framework provides a more storage-efficient solution. Specifically, we first identify a sparse set of motion-sensitive keypoints localized within motion regions using a view-space gradient difference strategy. Equipped with these keypoints, we propose an adaptive motion-driven mechanism that predicts a spatial influence field for propagating keypoint motion to neighboring Gaussian points with similar motion. Moreover, ComGS adopts an error-aware correction strategy for key frame reconstruction that selectively refines erroneous regions and mitigates error accumulation without unnecessary overhead. Overall, ComGS achieves a remarkable storage reduction of over $159 \times$ compared to 3DGSStream and $14 \times$ compared to the SOTA method QUEEN, while maintaining competitive visual fidelity and rendering speed. Our code will be released.

1 Introduction

Reconstructing free-viewpoint video (FVV) from multi-view videos captured by cameras with known poses has attracted growing interest in the field of computer vision and graphics. FVV exhibits great potential as a next-generation visual medium that enables immersive and interactive experiences, with broad application in virtual and augmented reality (VR/AR) applications [26].

Recently, 3D Gaussian Splatting (3DGS) has become a promising method for FVV reconstruction, due to its significant advancements in real-time rendering and high-fidelity view synthesis. These approaches typically fall into two categories: 1) incorporating temporal function into Gaussian primitives and optimizing directly [19, 34, 12], and 2) applying a deformation field to capture the spatio-temporal transformations of canonical Gaussians [18, 11, 37–39]. While these FVV reconstructions accurately represent dynamic scenes, they are trained in an offline manner and require transmitting the full set of reconstructed parameters prior to rendering.

In contrast, by enabling per-frame training and progressive transmission, online FVV reconstruction allows immediate playback without the overhead of full-scene preloading. As a pioneer work, 3DGStream [13] extends 3DGS to online FVV reconstruction using InstantNGP [4] to model the geometric transformation frame-by-frame. While achieving impressive rendering speed, its structural constraint hinders the volumetric representation performance and degrades the visual quality. Building on this paradigm, subsequent works [32, 33] enhance model expressiveness through explicitly optimizing Gaussian attribute residuals, achieving competitive synthesis quality and higher robustness. However, the storage demands of these methods remain prohibitively high for real-time transmission, with reconstructed data typically exceeding 20 MB per second.

In this paper, we aim to design a storage-efficient solution for FVV streaming that minimizes bandwidth requirements and enables real-time transmission. In online FVV reconstruction, since dynamic scenes contain a large proportion of static regions, the key to efficient reconstruction lies in motion modeling. Our first insight, therefore, is to only model the Gaussian attribute residuals in the motion regions, which eliminates the unnecessary updates in static regions. Building on motion modeling, we note that scene motion tends to be consistent, where Gaussian points associated with the same object typically exhibit the same or similar motion in dynamic scene representation. Our second insight, based on this observation, is to use a shared motion representation to model the attribute residuals with similar motion. This contrasts with existing online methods [13, 32] that utilize point-wise strategy to update the attribute residuals in motion regions, and the result is motion redundancy elimination and more compact storage. Lastly, we exploit a key frame fine-tune strategy to handle the error accumulation brought by non-rigid motion and novel objects emergence.

Specifically, to accomplish this, we propose a Compact Gaussian Streaming (ComGS) framework that leverages a set of keypoints ($= 200$), significantly fewer than the full set of Gaussian points ($\approx 200K$), to holistically model motion regions at each timestep. ComGS begins with a motion-sensitive keypoints selection through a view-space gradient difference strategy. This ensures that the selected keypoints are accurately positioned within motion regions and prevents redundant or incorrect modeling of static areas. Subsequently, we design an adaptive motion-driven mechanism that defines a keypoint-specific spatial influence field, with which neighboring Gaussian points can share the motion of the keypoint. Unlike conventional k -nearest neighbor (KNN) methods [43, 44], the spatial influence field can accommodate the complexity and variability of motion structure in dynamic scenes, so that keypoints can more accurately drive the motion of the surrounding region. Finally, to mitigate error accumulation in a compact and effective manner, we propose an error-aware correction strategy for key frame reconstruction that selectively updates only those Gaussians with reconstruction errors.

Our major contributions can be summarized as follow:

- We introduce a motion-sensitive keypoint selection to accurately identify keypoints within motion regions, and an adaptive motion-driven mechanism that effectively propagates motion to neighboring points. These leverage the locality and consistency of motion and achieve a more storage-efficient solution for online FVV reconstruction.
- We propose an error-aware correction strategy for key frame reconstruction that mitigates error accumulation over time by selectively updating Gaussian points with reconstruction errors, which ensures long-term consistency and minimizes redundant correction.

- Experiments on two benchmark datasets show that the effectiveness of our method and its individual components. Our method achieves a compression ratio of $159\times$ over the 3DGSStream and $14\times$ over state-of-the-art model QUEEN, enabling real-time transmission while preserving competitive reconstruction quality and rendering speed.

2 Related work

2.1 Dynamic Gaussian Splatting

Recently, 3D Gaussian Splatting (3DGS) [9, 10, 20–23] has attracted great attention in Free-viewpoint Video (FVV) reconstruction for its high photorealistic performance and real-time rendering speed. Several works [19, 34, 12] expand temporal variation as a function and optimize directly for modeling Gaussian attributes across frames. For instance, 4D Gaussian Splatting [19] incorporates time-conditioned 3D Gaussians and auxiliary components into 4D Gaussians, while ST-GS [12] models the transformation of structural attributes and opacity as a temporal function to represent scene motions. These time variant-based methods achieve superior rendering efficiency, but suffer from prohibitive storage requirements. Other works [11, 39–42] employ vanilla 3D Gaussians as a canonical space and a deformation field to represent the dynamic scene. In this category, 4D-GS [11] utilizes hexplanes [15], six orthogonal planes, as latent embeddings and deliver them into a small MLP to deform temporal transformation of Gaussian points, achieving efficient computational complexity and lightweight storage requirement. Building upon this, GD-GS [39] further improves scene modeling accuracy by incorporating geometric priors, which provides a more structured and precise representation of dynamic scene. Among them, both SC-GS [43] and SP-GS [44] adopt sparse control points to control scene motion using a k-nearest neighbor (KNN) [45] strategy for motion modeling. While these methods achieve notable improvements in computational efficiency and rendering speed, they are designed for offline FVV reconstruction and do not support frame-by-frame delivering. Additionally, motion-insensitive control point selection and scale-agnostic KNN motion modeling lead to redundant representation of static regions and reduced deformation accuracy in dynamic scenes. Our online method addresses these limitations by selecting keypoints from motion regions at each timestep and modeling motion with awareness of local motion scales, which enables more accurate and efficient modeling of online FVV.

2.2 Online Free-Viewpoint Video Reconstruction

Compared to the offline methods, online reconstruction enables FVV to be incrementally trained and transmitted in a per-frame manner, which allows users to preview or interact immediately with the video content. Leveraging the high-fidelity view synthesis capabilities of Neural Radiance Field (NeRF) [1–8], a set of studies have explored NeRF-based methods [25, 46, 47, 36, 29] for online FVV reconstruction, such as StreamRF [25], VideoRF [46] and TeTriRF [36]. Despite advanced visual quality, NeRF-based methods are hindered by their limited rendering speed of implicit structure, which limits their practical applications.

With the utilization of 3DGS [9], 3DGSStream [13] introduces a hash-based MLP to encode the position and rotation transformation of Gaussian points at each frame, and designs an adaptive Gaussians addition strategy for novel objects across frames. Based on this paradigm, QUEEN [32] proposes a Gaussian residual-based framework for model expressiveness enhancement and a learned quantization-sparsity framework for residuals compression. HiCoM [33] designs a hierarchical coherent motion mechanism to effectively capture and represent scene motion for fast and accurate training. To deploy into mobile device, V^3 [28] presents a novel approach that compresses Gaussian attributes as a 2D video to facilitate hardware video codecs. IGS [48] proposes a generalized anchor-driven Gaussian motion network that learns residuals with a single step, achieving a significant improvement of training speed. Nevertheless, these methods face challenge in real-time transmission, due to their substantial storage requirements. This overhead mainly stems from redundant updates of both static Gaussian points across frames, as well as repeated modeling of Gaussian points with similar motion. Our study exploits the locality and consistency of motion by leveraging motion-sensitive keypoints to adaptively drive motion regions, and this avoids redundant storage and transmission.

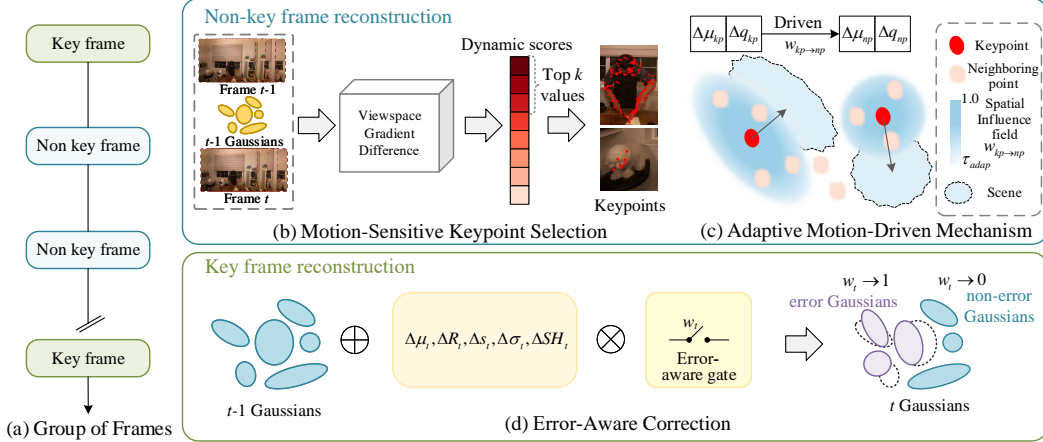


Figure 2: The overall pipeline of ComGS framework. (a) The reconstruction process starts from the first frame initialized using vanilla 3DGS [9]. Subsequent frames are organized into groups of frames (GoFs). For non-key frames, (b) we begins with a motion-sensitive keypoint selection using a viewspace gradient difference strategy, (c) and utilizes an adaptive motion-driven mechanism to control neighboring points motion. For key frames, (d) an error-aware correction strategy is introduced to mitigate the error accumulation across frames.

3 Methods

Our goal is to reconstruct and transmit FVV in a storage-efficient and streaming manner. To achieve it, we propose a Compact Gaussian Streaming (ComGS) framework for online FVV reconstruction, as illustrated in Fig. 2. First, ComGS begins with a motion-sensitivity keypoint selection using a viewspace gradient difference, ensuring subsequent motion control learning (Sec. 3.2). Second, we develop an adaptive motion-driven mechanism that applies a spatial influence field to control neighboring point motion (Sec. 3.3). Third, we devise an error-aware correction strategy for key frame reconstruction to mitigate error accumulation brought by non-rigid motion and novel objects emergence in online reconstruction (Sec. 3.4). Finally, we introduce our compression techniques and optimization process in Sec. 3.5.

3.1 Preliminary

3DGS [9] models a 3D scene as a large amount of anisotropic 3D Gaussian points in world space as an explicit representation. The central position and geometric shape of each Gaussian point in world space are defined by a mean vector μ and covariance matrix Σ , mathematically represented as:

$$G(x) = \exp\left(-\frac{1}{2}(\mathbf{x} - \mu)^T \Sigma^{-1}(\mathbf{x} - \mu)\right) \quad (1)$$

For differentiable optimization, the covariance matrix Σ is decoupled into a scaling matrix S and a rotation matrix R . Each Gaussian point is characterized by its color c_i and opacity α .

During rendering, the Gaussian points are initially projected into viewing plane, and the color of each pixel C can be obtained by α -blending:

$$C = \sum_{i \in n} c_i \alpha_i \prod_{j=1}^{i-1} (1 - \alpha_j) \quad (2)$$

where n is the number of Gaussian points contributing to this pixel.

3.2 Motion-Sensitive Keypoint Selection

Establishing an effective keypoint-driven motion representation necessitates to select appropriate keypoints. Considering motion locality, keypoints should be located in motion regions, which avoids redundant modeling in static areas and enables accurate modeling of complex motions

Thus, inspired by [32], we propose a motion-sensitive keypoint selection based on view-space gradient difference (Fig. 2 (b)). The core idea is to identify the dynamic Gaussian by the gradient change of rendering loss in inter-frames, and based on the gradient values, the k Gaussian points with the largest gradient are selected as keypoints. Specifically, following the gradient computation in 3DGS [9], we compute gradients using the previous Gaussian positions p_{t-1} , the rendered images R_{t-1} , the reconstruction loss \mathcal{L}_{recon} , and the ground-truth images GT_{t-1} and GT_t :

$$\mathcal{G}_{t-1} = \frac{\partial \mathcal{L}_{recon}^{t-1}}{\partial p_{t-1}}, \quad \mathcal{L}_{recon}^{t-1} = \mathcal{L}_{recon}(R_{t-1}, GT_{t-1}) \quad (3)$$

$$\mathcal{G}_t = \frac{\partial \mathcal{L}_{recon}^t}{\partial p_{t-1}}, \quad \mathcal{L}_{recon}^t = \mathcal{L}_{recon}(R_t, GT_t) \quad (4)$$

Dynamic significance scores $\Delta \mathcal{G}_t \in \mathbb{R}^N$ (N is the number of Gaussians) were calculated by means of absolute values of gradient differences:

$$\Delta \mathcal{G}_t = \frac{1}{V} \sum_{v=1}^V |\mathcal{G}_t^{(v)} - \mathcal{G}_{t-1}^{(v)}| \quad (5)$$

where V is the number of the training viewpoints. Finally, we select the top k high dynamic significance scores from all Gaussian points as keypoints \mathcal{K}_t at timestamp t . Selecting the top- k Gaussian points with the highest dynamic scores not only identifies those located in motion regions, but also naturally allocates more keypoints to the areas with complex motion, facilitating more accurate modeling of such regions.

In this paper, for a balance of training efficiency and reconstructed quality, we set $k = 200$.

3.3 Adaptive Motion-Driven Mechanism

Equipped with the selected keypoints \mathcal{K}_t at current timestep, the next step is to determine which neighboring points are controlled by these keypoints, and apply their transformations to drive the motion of the controlled neighboring points. Previous works [43, 44] employ k-nearest neighbor (KNN) [45] search to predict the motion of each Gaussian points, showing advanced results in monocular synthetic video reconstruction, but they do not fully consider unnecessary modeling in static region and motion scale difference, which leads to computational redundancy and inaccurate representation.

In contrast, we propose an adaptive motion-driven mechanism that enables each keypoint to drive neighboring points through a spatial influence field, as illustrated Fig. 2 (c). Specifically, motivated by [9], for each keypoints \mathcal{K}_t^i at t timestep, we initialize a quaternion $q_{adap}^i \in \mathbb{R}^4$ and a scaling vector $s_{adap}^i \in \mathbb{R}^3$ to compute the spatial influence field $\Sigma_{adap}^i \in \mathbb{R}^{3 \times 3}$. For a neighboring Gaussian point G_j with position μ_j , its distance to keypoint \mathcal{K}_t^i is given by $\mu_{ij} = \mu_j - \mu_{\mathcal{K}_t^i}$. The influence weight is then computed as:

$$w_{ij} = \exp\left(-\frac{1}{2} \mu_{ij}^\top (\Sigma_{adap}^i)^{-1} \mu_{ij}\right) \quad (6)$$

If w_{ij} exceeds a predefined threshold τ_{adap} , the Gaussian G_j is considered to be controlled by keypoint \mathcal{K}_t^i .

$$\text{If } w_{ij} \geq \tau_{adap}, \quad G_j \in \mathcal{C}_t^i \quad (7)$$

where \mathcal{C}_t^i denotes the set of Gaussians controlled by keypoint \mathcal{K}_t^i .

To model motion, each keypoint \mathcal{K}_t^i is further assigned a learnable translation offset $\Delta \mu_{\mathcal{K}}^i \in \mathbb{R}^3$ and a rotation represented by a quaternion $\Delta q_{\mathcal{K}}^i \in \mathbb{R}^4$. For a Gaussian G_j controlled by multiple keypoints $\{\mathcal{K}_t^i\}_{i \in \mathcal{I}_j}$, its overall motion is computed by aggregating the motions of its associated keypoints, weighted by their influence scores w_{ij} :

$$\Delta \mu_j^t = \sum_{i \in \mathcal{I}_j} w_{ij} \cdot \Delta \mu_{\mathcal{K}}^i, \quad \Delta q_j^t = \sum_{i \in \mathcal{I}_j} w_{ij} \cdot \Delta q_{\mathcal{K}}^i \quad (8)$$

where $\Delta \mu_j^t$ and Δq_j^t indicate the motion of Gaussian j at t timestep.

By leveraging a compact set of keypoints with spatial influence fields, our method enables accurate and efficient control of Gaussian motions at each frame. Since Gaussians share motion attributes through keypoints, only 14 parameters per keypoint are required, significantly reducing storage demands and mitigating data redundancy.

3.4 Error-Aware Corrector

By using keypoints to drive scene motion, we model the transformation of Gaussian points from the previous frame to the current frame with an extremely compact parameters. Nevertheless, keypoints-based motion controlling only supports to represent rigid motion effectively and faces challenge to handle non-rigid motion and novel objects emergence, which results in error accumulation across frames.

A straightforward solution to mitigate error accumulation and ensure accurate long-term FVV representations is to separate the video into frame groups and update the attributes of all Gaussians at key frames. However, this strategy would lead to a substantial of unnecessary parameters updating, since most of parameters are already correctly representing the scene and do not require modification. To mitigate error accumulation in a compact and efficient manner, we propose an error-aware corrector strategy that only finetunes the Gaussians with detected errors, significantly decreasing storage demands and promoting more accurate scene reconstruction, as illustrated in Fig. 2 (d).

Specifically, given a video sequence, we select a key frame every s frames, forming the key frame sequence $\{f_s, f_{2s}, \dots, f_{ns}\}$, as shown in Fig. 2 (a). The remaining frames are reconstructed by keypoints driven. During key frame reconstruction, given the attributes of a Gaussian point at previous timestep $\theta_i^{t-1} : (\mu_i^{t-1}, q_i^{t-1}, s_i^{t-1}, \sigma_i^{t-1}, sh_i^{t-1})$, we introduce a set of learnable parameters $\Delta\theta_i^t$ to model the attribute residuals. To identify which Gaussian points require correction, we predict a learnable mask m_i for each point. A sigmoid function is used to map m_i to the range $(0, 1)$, which refers as a soft mask:

$$m_i^{soft} = \text{Sigmoid}(m_i), m_i^{soft} \in (0, 1) \quad (9)$$

Similar to [21, 22], the soft mask is binarized into a hard mask using a predefined threshold ϕ_{thres} , where the non-differentiable binarization is handled with the straight-through estimator (STE) to enable gradient flow, represented as:

$$m_i^{hard} = sg(\mathbb{1}(m_i^{soft} > \phi_{thres}) - m_i^{soft}) + m_i^{soft}, m_i^{hard} \in \{0, 1\} \quad (10)$$

where $\mathbb{1}$ is the indicator function and sg indicates the stop gradient operation. Then, the m_i^{hard} is applied to the attribute residuals before rendering, followed as:

$$\theta_i^t = \theta_i^{t-1} \oplus m_i^{hard} * \Delta\theta_i^t \quad (11)$$

where \oplus denotes the attribute-specific update operation. Meanwhile, we define a optimized function to regulate the perceptual error while encouraging sparse residual updates:

$$\mathcal{L}_{error} = \frac{1}{N} \sum_i m_i^{soft} \quad (12)$$

After optimization for the current key frame, only the attribute residuals $\hat{\Delta\theta}^t = \{\Delta\theta^t | \mathcal{M}^{hard} = 1\}$ and the hard mask set \mathcal{M}^{hard} need to be stored and transmitted, minimizing the required data redundancy and transmission overhead.

3.5 Optimization and Compression

For the first frame optimization, we employ COLMAP [27] to generate the initial point cloud and follow the pipeline of 3DGStream [13]. The optimization for both the first frame and non-key frames is supervised by the reconstruction loss \mathcal{L}_{recon} , which is composed by an L_1 -norm loss \mathcal{L}_1 and a D-SSIM loss \mathcal{L}_{D-SSIM} [24]:

$$\mathcal{L}_{recon} = (1 - \lambda_{D-SSIM})\mathcal{L}_1 + \lambda_{D-SSIM}\mathcal{L}_{D-SSIM} \quad (13)$$

For key frame optimization, we minimize a combined loss consisting of \mathcal{L}_{recon} and \mathcal{L}_{error} :

$$\mathcal{L}_{total} = \mathcal{L}_{recon} + \lambda_{error}\mathcal{L}_{error} \quad (14)$$

Table 1: Quantitative comparisons on Neural 3D Video (N3DV) [14] and MeetRoom datasets [25].

| Dataset | Category | Method | PSNR (dB) \uparrow | Storage (MB) \downarrow | Training (sec) \downarrow | Rendering (FPS) \uparrow |
|----------|----------|-----------------|----------------------|---------------------------|-----------------------------|----------------------------|
| N3DV | Offline | NeRFPlayer [29] | 30.69 | 17.10 | 72 | 0.05 |
| | | HyperReel [30] | 31.10 | 1.20 | 104 | 2.00 |
| | | 4DGS [11] | 31.15 | 0.13 | 8 | 34 |
| | | SpaceTime [12] | 32.05 | 0.67 | 20 | 140 |
| | Online | StreamRF [25] | 30.68 | 31.4 | 15 | 8.3 |
| | | TeTriRF [36] | 30.43 | 0.06 | 39 | 4 |
| | | 3DGStream [13] | 31.67 | 7.80 | 8.5 | 261 |
| | | QUEEN-s [32] | 31.89 | 0.68 | 4.65 | 345 |
| | | QUEEN-l [32] | 32.19 | 0.75 | 7.9 | 248 |
| | | ComGS-s (ours) | 31.87 | 0.049 | 37 | 91 |
| MeetRoom | Static | I-NGP [35] | 28.10 | 48.2 | 66 | 4.1 |
| | | 3DG-S [9] | 31.31 | 21.1 | 156 | 571 |
| | Online | StreamRF [25] | 26.72 | 9.0 | 10.2 | 10 |
| | | 3DGStream [13] | 30.79 | 4.1 | 4.9 | 350 |
| | | ComGS-s (ours) | 31.49 | 0.028 | 28.3 | 98 |

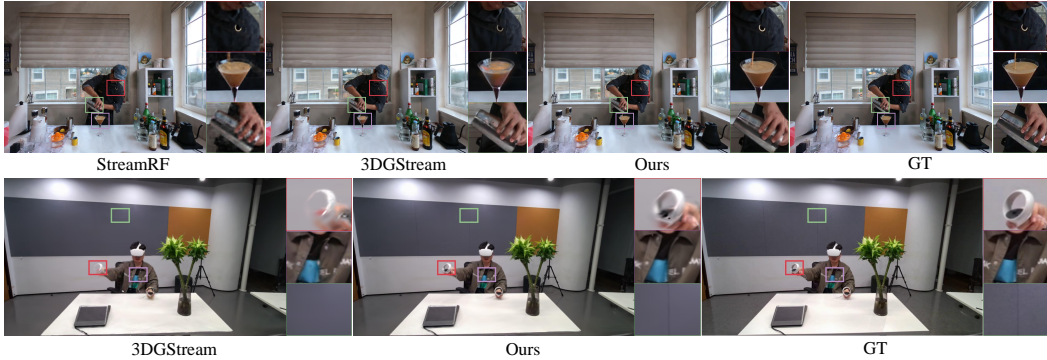


Figure 3: Quantitative comparison. We visualize our method and other online FVV methods on N3DV [14] and MeetRoom [25] dataset.

where λ_{error} controls the degree of error awareness, thereby balancing reconstruction quality and memory efficiency. We set $\lambda_{D-SSIM} = 0.2$ and $\lambda_{error} = 0.001$ in this paper.

After optimization, the initialized Gaussians θ^0 and the residuals $\Delta\hat{\theta}^t$ for key frame error correction are further compressed through quantization and entropy coding, enabling compact storage without performance degradation. More details are provided in the **Appendix**.

Table 2: Ablation study on proposed components. Flame Steak and Flame Salmon are from the N3DV dataset.

| Experiments | Selection | Adaptive | Correction | Flame Steak | | Flame Salmon | |
|-------------|-----------|----------|------------|----------------------|---------------------------|----------------------|---------------------------|
| | | | | PSNR (dB) \uparrow | Storage (KB) \downarrow | PSNR (dB) \uparrow | Storage (KB) \downarrow |
| 1 | × | ✓ | ✓ | 33.27 | 46.7 | 29.22 | 56.7 |
| 2 | ✓ | × | ✓ | 32.82 | 36.4 | 28.96 | 45.7 |
| 3 | × | × | ✓ | 31.26 | 37.9 | 27.75 | 46.4 |
| 4 | ✓ | ✓ | × | 31.67 | 26.9 | 28.74 | 26.9 |
| 5 | ✓ | ✓ | ✓ | 33.49 | 46.5 | 29.32 | 53.4 |

4 Experiments

4.1 Experimental Setup

We evaluate our method on two widely-used public benchmark datasets. (1) **Neural 3D Video (N3DV)** [14] consists of six indoor video sequences captured by 18 to 21 viewpoints. (2) **Meet**



Figure 4: Visualization of our keypoint-driven motion representation. **Top**: selected keypoints are concentrated in motion regions. **Bottom**: adaptive control of neighboring points also focuses on motion-intensive areas, enabling accurate and efficient motion modeling.



Figure 5: Visualization of different selection methods and corresponding updated regions.

Room [25] comprises four indoor scenes recorded with a 13 cameras multi-view system. In both of two datasets, we employ the first view for testing. Our method is implemented on an NVIDIA A100 GPU. We train 150 epochs for non-key frames reconstruction and 1000 epochs for key frames fine-tuning. We measure the visual quality of rendered images by average PSNR, required storage, rendering FPS and training time. More implement details are provided in the **Appendix**.

4.2 Quantitative Comparisons

We conduct quantitative comparisons on existing online methods including StreamRF [25], TeTriRF [36], 3DGStream [13] and QUEEN [32], as well as the SOTA offline FVV approaches [12, 11, 29, 30] on N3DV and Meetroom (Tab. 1). Our method is evaluated in two variants: ComGS-s (small) and ComGS-l (large), using key frame intervals of $s=10$ and $s=2$, respectively.

Tab. 1 shows that our ComGS achieves competitive results among existing online FVV methods on N3DV dataset. Notably, ComGS-s achieves a substantial reduction in storage by $159\times$ compared to 3DGStream and $14\times$ compared to QUEEN. This advantage enables real-time transmission in limited bandwidth and enhances the overall user viewing experience. On MeetRoom dataset, our method outperforms 3DGStream, obtaining $+0.7\text{dB}$ PSNR and $146\times$ smaller size. Our advantages are mainly due to two factor: 1) using keypoint as a shared representation requires transmitting only a small number of keypoint attributes; and 2) the error-aware correction module effectively rectifies regions with scene inaccuracies using minimal additional parameters. In the **Appendix**, the quantitative results are provided for each scene to offer a more detailed comparison.

4.3 Qualitative Comparisons

As shown in Fig. 3, we compare our reconstructed results to other online FVV methods on N3DV and MeetRoom. ComGS effectively reconstructs both motion and static regions and provides more closer results to the ground truth. Fig. 3 shows that 3DGStream introduces noticeable artifacts due to its global update of Gaussian points across the entire scene, which often leads to incorrect updates in static regions. In contrast, our method restricts modeling to motion regions and applies targeted corrections in error-prone areas, resulting in more accurate and robust scene reconstruction. More qualitative results are offered in **Appendix**.

4.4 Ablation Study

To validate the effectiveness of our proposed methods, we ablate three components of ComGS framework in Tab. 2. In the Experiment 1, we adopt a random chosen techniques for keypoint



Figure 6: (a) PSNR comparison over time. Visualizations of (b) w/o key frames correction. (c) ComGS-s. (d) ComGS-l.

selection. However, since the selection is not guided by region regions, it may result in ineffective modeling of static areas and inadequate representation of scenes, which leads to a slight degradation in PSNR. Experiment 2 model scene motion only using the selected keypoints, without applying the adaptive motion-driven mechanism for neighboring points. The resulting drop in reconstruction quality demonstrates the importance of collaborative modeling in keypoint-driven regions for accurate motion representation. In the Experiment 3, we reconstruct the FVV only relying on the key frames correction, which indicates that keypoint-driven motion representation is crucial for our method. Experiment 4 disable the error-aware correction in key frames reconstruction. This leads to a significant performance drop, demonstrating that error-aware correction in key frames would solve the error accumulation across frames.

Table 3: Ablation study on comparing control strategies for neighboring points.

| Control tech | PSNR (dB) | Storage (KB) |
|--------------|--------------|--------------|
| KNN | 31.39 | 44.1 |
| Adaptive | 31.87 | 49.0 |

Table 4: Ablation study of the error-aware correction strategy.

| Configuration | PSNR (dB) | Storage (KB) |
|------------------|--------------|--------------|
| w/o error-aware | 31.65 | 373 |
| with error-aware | 31.87 | 49.0 |

To further investigate the role of keypoint-driven motion representation, we visualize the selection and driven process in Fig. 4. The top row shows that keypoints are predominantly selected in motion regions, such as the human body and moving objects. The bottom row highlights the adaptively controlled areas for neighboring points, which similarly focus on regions with significant motion (e.g., the person and the dog). Fig. 5 visualizes Gaussians updated region using farthest keypoint selection [44], random keypoint selection and our method, respectively, which demonstrates that our method accurately captures motion-intensive areas. These results indicate that ComGS can effectively leverage the locality and consistency of scene motion.

We also evaluate a KNN-based method [45] for selecting neighboring points around keypoints (Tab. 3). This approach shows inferior performance, as it does not distinguish between static and motion regions, leading to redundant modeling and poor adaptation to varying motion scales.

Fig. 6 evaluates the effect of key frame correction. The visual results in Fig. 6 (b–d) further highlight that key frame correction significantly reduces artifacts in motion regions such as flames, helping to maintain finer temporal consistency throughout the sequence. Tab. 4 shows that correction without error-aware leads to significantly higher storage due to redundant Gaussians updating. Moreover, without focusing on high-error regions, updates may affect error-free areas and result in suboptimal performance. Therefore, enabling error-awareness improves both accuracy and efficiency.

5 Conclusion

In this paper, we proposed ComGS, a storage-efficient framework for online FVV real-time transmission. We utilized a keypoint-driven motion representation to models scene motion by leveraging the locality and consistency of motion. This approach significantly reduces storage requirements through motion-sensitive keypoint selection and an adaptive motion driven mechanism. To address error accumulation over time, we further introduce an error-aware correction strategy that mitagates these

error in an efficient manner. Experiments demonstrate the surpassing storage efficiency, competitive visual fidelity and rendering speed of our method. In future work, we aim to design a practical solution on novel applications, such as 3D video conference and volumetric live streaming, providing viewers with immersive and interactive experiences.

References

- [1] B. Mildenhall, P. P. Srinivasan, M. Tancik, J. T. Barron, R. Ramamoorthi, and R. Ng, “Nerf: Representing scenes as neural radiance fields for view synthesis,” *Communications of the ACM*, vol. 65, no. 1, pp. 99–106, 2021.
- [2] A. Chen, Z. Xu, A. Geiger, J. Yu, and H. Su, “Tensorf: Tensorial radiance fields,” in *European conference on computer vision*. Springer, 2022, pp. 333–350.
- [3] S. Fridovich-Keil, A. Yu, M. Tancik, Q. Chen, B. Recht, and A. Kanazawa, “Plenoxels: Radiance fields without neural networks,” in *Proceedings of the IEEE/CVF conference on computer vision and pattern recognition*, 2022, pp. 5501–5510.
- [4] T. Müller, A. Evans, C. Schied, and A. Keller, “Instant neural graphics primitives with a multiresolution hash encoding,” *ACM transactions on graphics (TOG)*, vol. 41, no. 4, pp. 1–15, 2022.
- [5] A. Chen, Z. Xu, X. Wei, S. Tang, H. Su, and A. Geiger, “Dictionary fields: Learning a neural basis decomposition,” *ACM Transactions on Graphics (TOG)*, vol. 42, no. 4, pp. 1–12, 2023.
- [6] C. Sun, M. Sun, and H.-T. Chen, “Direct voxel grid optimization: Super-fast convergence for radiance fields reconstruction,” in *Proceedings of the IEEE/CVF conference on computer vision and pattern recognition*, 2022, pp. 5459–5469.
- [7] J. T. Barron, B. Mildenhall, M. Tancik, P. Hedman, R. Martin-Brualla, and P. P. Srinivasan, “Mip-nerf: A multiscale representation for anti-aliasing neural radiance fields,” in *Proceedings of the IEEE/CVF international conference on computer vision*, 2021, pp. 5855–5864.
- [8] D. Verbin, P. Hedman, B. Mildenhall, T. Zickler, J. T. Barron, and P. P. Srinivasan, “Ref-nerf: Structured view-dependent appearance for neural radiance fields,” in *2022 IEEE/CVF Conference on Computer Vision and Pattern Recognition (CVPR)*. IEEE, 2022, pp. 5481–5490.
- [9] B. Kerbl, G. Kopanas, T. Leimkühler, and G. Drettakis, “3d gaussian splatting for real-time radiance field rendering,” *ACM Trans. Graph.*, vol. 42, no. 4, pp. 139–1, 2023.
- [10] Z. Fan, K. Wang, K. Wen, Z. Zhu, D. Xu, and Z. Wang, “Lightgaussian: Unbounded 3d gaussian compression with 15x reduction and 200+ fps,” *arXiv preprint arXiv:2311.17245*, 2023.
- [11] G. Wu, T. Yi, J. Fang, L. Xie, X. Zhang, W. Wei, W. Liu, Q. Tian, and X. Wang, “4d gaussian splatting for real-time dynamic scene rendering,” in *Proceedings of the IEEE/CVF Conference on Computer Vision and Pattern Recognition*, 2024, pp. 20 310–20 320.
- [12] Z. Li, Z. Chen, Z. Li, and Y. Xu, “Spacetime gaussian feature splatting for real-time dynamic view synthesis,” in *Proceedings of the IEEE/CVF Conference on Computer Vision and Pattern Recognition*, 2024, pp. 8508–8520.
- [13] J. Sun, H. Jiao, G. Li, Z. Zhang, L. Zhao, and W. Xing, “3dstream: On-the-fly training of 3d gaussians for efficient streaming of photo-realistic free-viewpoint videos,” in *Proceedings of the IEEE/CVF Conference on Computer Vision and Pattern Recognition*, 2024, pp. 20 675–20 685.
- [14] T. Li, M. Slavcheva, M. Zollhoefer, S. Green, C. Lassner, C. Kim, T. Schmidt, S. Lovegrove, M. Goesele, R. Newcombe *et al.*, “Neural 3d video synthesis from multi-view video,” in *Proceedings of the IEEE/CVF Conference on Computer Vision and Pattern Recognition*, 2022, pp. 5521–5531.
- [15] A. Cao and J. Johnson, “Hexplane: A fast representation for dynamic scenes,” in *Proceedings of the IEEE/CVF Conference on Computer Vision and Pattern Recognition*, 2023, pp. 130–141.
- [16] Z. Li, S. Niklaus, N. Snavely, and O. Wang, “Neural scene flow fields for space-time view synthesis of dynamic scenes,” in *Proceedings of the IEEE/CVF Conference on Computer Vision and Pattern Recognition*, 2021, pp. 6498–6508.

- [17] S. Fridovich-Keil, G. Meanti, F. R. Warburg, B. Recht, and A. Kanazawa, “K-planes: Explicit radiance fields in space, time, and appearance,” in *Proceedings of the IEEE/CVF Conference on Computer Vision and Pattern Recognition*, 2023, pp. 12 479–12 488.
- [18] Z. Yang, X. Gao, W. Zhou, S. Jiao, Y. Zhang, and X. Jin, “Deformable 3d gaussians for high-fidelity monocular dynamic scene reconstruction,” in *Proceedings of the IEEE/CVF Conference on Computer Vision and Pattern Recognition*, 2024, pp. 20 331–20 341.
- [19] Z. Yang, H. Yang, Z. Pan, and L. Zhang, “Real-time photorealistic dynamic scene representation and rendering with 4d gaussian splatting,” *arXiv preprint arXiv:2310.10642*, 2023.
- [20] K. Navaneet, K. P. Meibodi, S. A. Koohpayegani, and H. Pirsivash, “Compact3d: Compressing gaussian splat radiance field models with vector quantization,” *arXiv preprint arXiv:2311.18159*, 2023.
- [21] J. C. Lee, D. Rho, X. Sun, J. H. Ko, and E. Park, “Compact 3d gaussian representation for radiance field,” in *Proceedings of the IEEE/CVF Conference on Computer Vision and Pattern Recognition*, 2024, pp. 21 719–21 728.
- [22] H. Wang, H. Zhu, T. He, R. Feng, J. Deng, J. Bian, and Z. Chen, “End-to-end rate-distortion optimized 3d gaussian representation,” in *European Conference on Computer Vision*. Springer, 2025, pp. 76–92.
- [23] P. Papanatakis, G. Kopanas, B. Kerbl, A. Lanvin, and G. Drettakis, “Reducing the memory footprint of 3d gaussian splatting,” *Proceedings of the ACM on Computer Graphics and Interactive Techniques*, vol. 7, no. 1, pp. 1–17, 2024.
- [24] Z. Wang, A. C. Bovik, H. R. Sheikh, and E. P. Simoncelli, “Image quality assessment: from error visibility to structural similarity,” *IEEE transactions on image processing*, vol. 13, no. 4, pp. 600–612, 2004.
- [25] L. Li, Z. Shen, Z. Wang, L. Shen, and P. Tan, “Streaming radiance fields for 3d video synthesis,” *Advances in Neural Information Processing Systems*, vol. 35, pp. 13 485–13 498, 2022.
- [26] Y. Chen, Q. Wang, H. Chen, X. Song, H. Tang, and M. Tian, “An overview of augmented reality technology,” in *Journal of Physics: Conference Series*, vol. 1237, no. 2. IOP Publishing, 2019, p. 022082.
- [27] J. L. Schonberger and J.-M. Frahm, “Structure-from-motion revisited,” in *Proceedings of the IEEE conference on computer vision and pattern recognition*, 2016, pp. 4104–4113.
- [28] P. Wang, Z. Zhang, L. Wang, K. Yao, S. Xie, J. Yu, M. Wu, and L. Xu, “V³: Viewing volumetric videos on mobiles via streamable 2d dynamic gaussians,” *ACM Transactions on Graphics (TOG)*, vol. 43, no. 6, pp. 1–13, 2024.
- [29] L. Song, A. Chen, Z. Li, Z. Chen, L. Chen, J. Yuan, Y. Xu, and A. Geiger, “Nerfplayer: A streamable dynamic scene representation with decomposed neural radiance fields,” *IEEE Transactions on Visualization and Computer Graphics*, vol. 29, no. 5, pp. 2732–2742, 2023.
- [30] B. Attal, J.-B. Huang, C. Richardt, M. Zollhofer, J. Kopf, M. O’Toole, and C. Kim, “Hyper-reel: High-fidelity 6-dof video with ray-conditioned sampling,” in *Proceedings of the IEEE/CVF Conference on Computer Vision and Pattern Recognition*, 2023, pp. 16 610–16 620.
- [31] D. A. Huffman, “A method for the construction of minimum-redundancy codes,” *Proceedings of the IRE*, vol. 40, no. 9, pp. 1098–1101, 1952.
- [32] S. Girish, T. Li, A. Mazumdar, A. Shrivastava, S. De Mello *et al.*, “Queen: Quantized efficient encoding of dynamic gaussians for streaming free-viewpoint videos,” *Advances in Neural Information Processing Systems*, vol. 37, pp. 43 435–43 467, 2025.
- [33] Q. Gao, J. Meng, C. Wen, J. Chen, and J. Zhang, “Hicom: Hierarchical coherent motion for dynamic streamable scenes with 3d gaussian splatting,” in *The Thirty-eighth Annual Conference on Neural Information Processing Systems*.

- [34] J. Luiten, G. Kopanas, B. Leibe, and D. Ramanan, “Dynamic 3d gaussians: Tracking by persistent dynamic view synthesis,” in *2024 International Conference on 3D Vision (3DV)*. IEEE, 2024, pp. 800–809.
- [35] Y. Jiang, K. Yao, Z. Su, Z. Shen, H. Luo, and L. Xu, “Instant-nvr: Instant neural volumetric rendering for human-object interactions from monocular rgbd stream,” in *Proceedings of the IEEE/CVF Conference on Computer Vision and Pattern Recognition*, 2023, pp. 595–605.
- [36] M. Wu, Z. Wang, G. Kourois, and T. Tuytelaars, “Tetrif: Temporal tri-plane radiance fields for efficient free-viewpoint video,” in *Proceedings of the IEEE/CVF conference on computer vision and pattern recognition*, 2024, pp. 6487–6496.
- [37] Z. Lu, X. Guo, L. Hui, T. Chen, M. Yang, X. Tang, F. Zhu, and Y. Dai, “3d geometry-aware deformable gaussian splatting for dynamic view synthesis,” in *Proceedings of the IEEE/CVF Conference on Computer Vision and Pattern Recognition*, 2024, pp. 8900–8910.
- [38] M. Liu, Q. Yang, H. Huang, W. Huang, Z. Yuan, Z. Li, and Y. Xu, “Light4gs: Lightweight compact 4d gaussian splatting generation via context model,” *arXiv preprint arXiv:2503.13948*, 2025.
- [39] J. Bae, S. Kim, Y. Yun, H. Lee, G. Bang, and Y. Uh, “Per-gaussian embedding-based deformation for deformable 3d gaussian splatting,” in *European Conference on Computer Vision*. Springer, 2024, pp. 321–335.
- [40] W. O. Cho, I. Cho, S. Kim, J. Bae, Y. Uh, and S. J. Kim, “4d scaffold gaussian splatting for memory efficient dynamic scene reconstruction,” *arXiv preprint arXiv:2411.17044*, 2024.
- [41] D. Sun, H. Guan, K. Zhang, X. Xie, and S. K. Zhou, “Sdd-4dgs: Static-dynamic aware decoupling in gaussian splatting for 4d scene reconstruction,” *arXiv preprint arXiv:2503.09332*, 2025.
- [42] J. Yan, R. Peng, L. Tang, and R. Wang, “4d gaussian splatting with scale-aware residual field and adaptive optimization for real-time rendering of temporally complex dynamic scenes,” in *Proceedings of the 32nd ACM International Conference on Multimedia*, 2024, pp. 7871–7880.
- [43] Y.-H. Huang, Y.-T. Sun, Z. Yang, X. Lyu, Y.-P. Cao, and X. Qi, “Sc-gs: Sparse-controlled gaussian splatting for editable dynamic scenes,” in *Proceedings of the IEEE/CVF conference on computer vision and pattern recognition*, 2024, pp. 4220–4230.
- [44] D. Wan, R. Lu, and G. Zeng, “Superpoint gaussian splatting for real-time high-fidelity dynamic scene reconstruction,” in *Proceedings of the 41st International Conference on Machine Learning*, 2024, pp. 49 957–49 972.
- [45] L. E. Peterson, “K-nearest neighbor,” *Scholarpedia*, vol. 4, no. 2, p. 1883, 2009.
- [46] L. Wang, K. Yao, C. Guo, Z. Zhang, Q. Hu, J. Yu, L. Xu, and M. Wu, “Videorf: Rendering dynamic radiance fields as 2d feature video streams,” in *Proceedings of the IEEE/CVF Conference on Computer Vision and Pattern Recognition*, 2024, pp. 470–481.
- [47] L. Wang, Q. Hu, Q. He, Z. Wang, J. Yu, T. Tuytelaars, L. Xu, and M. Wu, “Neural residual radiance fields for streamably free-viewpoint videos,” in *Proceedings of the IEEE/CVF Conference on Computer Vision and Pattern Recognition*, 2023, pp. 76–87.
- [48] J. Yan, R. Peng, Z. Wang, L. Tang, J. Yang, J. Liang, J. Wu, and R. Wang, “Instant gaussian stream: Fast and generalizable streaming of dynamic scene reconstruction via gaussian splatting,” *arXiv preprint arXiv:2503.16979*, 2025.

Appendix

We provide more material to supplement our main paper. This appendix first introduces more implementation details in Sec. A. Then, we provide additional experimental results in Sec. B, discussion on limitations and future works in Sec. C and broader impact in Sec. D.

A More Implementation details

Training: Our code is based on the open-source code of 3DGStream [13]. On both N3DV and MeetRoom dataset, we utilize COLMAP [27] to generate the initial point cloud and vanilla 3DGS [9] to initialize the Gaussians for 3000 epochs at first frame. Subsequently, our ComGS reconstructs the non key frames for 150 epochs and key frames for 1000 epochs. For the balance of visual quality and storage requirements, we set spherical harmonics (SH) degree to 1. During training, the learning rate for Gaussian attributes is set to 0.002, for the attributes of the adaptive influence region to 0.02, and for the learnable mask m_i to 0.01. Other learning rates follow the setting of 3DGStream [13].

Compression: For the reconstruction process, the uncompressed Gaussian attributes and their residuals have substantial memory requirements. We employ quantization and entropy coding to further compress them. Specifically, for the first frame reconstruction, we apply 16-bit quantization to the position attributes due to their higher sensitivity, while the other attributes are quantized to 8 bits. For the correction in key frame reconstruction, we quantize all attribute residuals using 8 bits. Notably, the attributes of a keypoint play a crucial role in guiding the motion of nearby non-keypoints. As a result, even minor quantization errors in keypoints may be amplified throughout the scene. To preserve modeling accuracy, we thus refrain from quantizing keypoint attributes. Finally, we deliver these quantized values to entropy coding [31].

Datasets: (1) Neural 3D Video (N3DV) dataset [14] comprises of six indoor scenes captured by a multi-view system of 18 to 21 cameras at a resolution of 2704×2028 and 30 FPS. Following the previous works [13, 14, 11], we downsample the videos by a factor of 2 for training and testing and employ the central view for testing view. **(2) MeetRoom dataset** [25] is captured by a 13-camera multi-view system, including four dynamic scenes at 1280×720 resolution and 30 FPS. The center reference camera is also used for testing. We perform distortion for this dataset following the settings of the 3DGS [9] to improve the reconstruction quality.

Table 5: Ablation study on Number of keypoints.

| #Keypoints | 50 | 100 | 200 | 300 | 400 | 500 |
|----------------------------|-------|-------|-------|-------|-------|-------|
| PSNR (dB \uparrow) | 31.77 | 31.85 | 31.87 | 31.84 | 31.86 | 31.80 |
| Storage (KB \downarrow) | 44.4 | 46.2 | 50.1 | 50.2 | 54.4 | 57.3 |

Table 6: Ablation study on Group of Frames.

| #Frames | 2 | 5 | 10 | 15 | 20 |
|----------------------------|-------|-------|-------|-------|-------|
| PSNR (dB \uparrow) | 32.12 | 32.01 | 31.87 | 31.78 | 31.66 |
| Storage (KB \downarrow) | 108.3 | 66.6 | 50.1 | 43.2 | 40.0 |

B Additional Experimental Results

B.1 More Ablation Study

In this section, we further investigate the hyperparameters and analyze the impact of the proposed components on N3DV [14] dataset, to achieve a balance between performance and efficiency.

Effect of the keypoint numbers: To investigate the impact of the number of keypoints on reconstruction quality and compression efficiency, we conduct an ablation study by varying the number of keypoints from 50 to 500. As shown in Tab. 5, the reconstruction performance peaks when using 200 keypoints. This observation aligns with the nature of dynamic scenes, where motion typically

Table 7: Effect of λ_{error} on reconstructed quality and storage.

| λ_{error} | 0 | 0.0001 | 0.001 | 0.01 |
|----------------------------|-------|--------|-------|-------|
| PSNR (dB \uparrow) | 31.91 | 31.91 | 31.87 | 31.79 |
| Storage (KB \downarrow) | 183.0 | 96.3 | 50.1 | 29.2 |

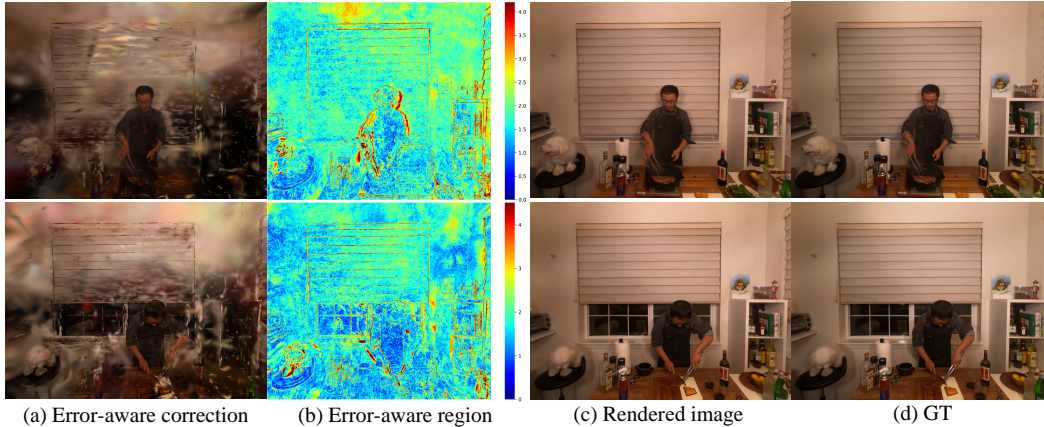


Figure 7: (a) Visualization of error-aware Gaussians. (b) Visualization of error regions between key frame and previous frame. (c)(d) Comparison on rendered images and original images.

occurs in a limited spatial region. Using 200 keypoints is sufficient to capture these areas for effective reconstruction. Increasing the number of keypoints beyond this leads to redundant or incorrect representation in static regions. Therefore, using 200 keypoints strikes a good balance between performance and storage, and is adopted as the default configuration in our method.

Effect of group of frames: We evaluate how the size of the Group of Frames (GoF) affects reconstruction quality and storage, as shown in Tab. 6. These results indicate that shorter GoFs can better handle non-rigid motions and novel objects, which are difficult to be reconstructed by keypoint-driven motion. Larger GoFs exploit temporal redundancy for better compression, but may accumulate errors in the presence of motion and scene changes. In our setting, we use $GoF = 2$ as our *large* model for high-fidelity reconstruction, and $GoF = 10$ as our *small* model for compact representation.

Effect of error-aware correction: We explore the effect of the parameter λ_{error} on reconstruction quality and storage, as shown in Tab. 7. While a larger λ_{error} improves compression by focusing only on perceptually salient errors, it may overlook subtle regions, which leads to degraded reconstruction. In contrast, smaller values retain more points, which helps suppress error accumulation across frames, albeit with higher storage costs.

Fig. 7 (a) visualizes the error-aware Gaussian points identified by error-aware correction, while (b) shows a heatmap of differences between the key frame and the previous frame, which highlights the error regions. We observe that the error-aware points in (a) align well with the high-error regions in (b), which indicates that our method effectively captures areas likely to suffer from error accumulation. Fig. 7 (c) and (d) compare our rendered images with the ground truth. The results show that our method significantly reduces artifacts in dynamic regions, confirming the effectiveness of our error-aware correction.

B.2 More Results

To offer a more comprehensive comparison, the per-scene quantitative results are presented on N3DV [14] and MeetRoom [25] in Tab. 8 and Tab. 9, respectively. Moreover, we also provide the experimental results of existing offline and online methods in Tab. 8 as a reference. Further qualitative results with StreamRF [25] and 3DGStream [13] are indicated in Fig. 8 and Fig. 9.

Table 8: **Per-scene quantitative results on the N3DV dataset.** Offline and online methods are separated for clarity.

| Method | Coffee Martini | | Cook Spinach | | Cut Beef | |
|-------------------|-----------------------|----------------------------|-----------------------|----------------------------|-----------------------|----------------------------|
| | PSNR (dB \uparrow) | Storage (MB \downarrow) | PSNR (dB \uparrow) | Storage (MB \downarrow) | PSNR (dB \uparrow) | Storage (MB \downarrow) |
| KPlanes [17] | 29.99 | 1.0 | 32.60 | 1.0 | 31.82 | 1.0 |
| NeRFPlayer [29] | 31.53 | 18.4 | 30.56 | 18.4 | 29.35 | 18.4 |
| HyperReel [30] | 28.37 | 1.2 | 32.30 | 1.2 | 32.92 | 1.2 |
| 4DGS [19] | 28.33 | 29.0 | 32.93 | 29.0 | 33.85 | 29.0 |
| 4D-GS [11] | 27.34 | 0.3 | 32.46 | 0.3 | 32.49 | 0.3 |
| Spacetime-GS [12] | 28.61 | 0.7 | 33.18 | 0.7 | 33.52 | 0.7 |
| E-D3DGS [39] | 29.33 | 0.5 | 33.19 | 0.5 | 33.25 | 0.5 |
| StreamRF [25] | 27.84 | 31.84 | 31.59 | 31.84 | 31.81 | 31.84 |
| 3DGStream [13] | 27.75 | 7.80 | 33.31 | 7.80 | 33.21 | 7.80 |
| QUEEN-I [32] | 28.38 | 1.17 | 33.40 | 0.59 | 34.01 | 0.57 |
| ComGS-s (ours) | 28.63 | 0.058 | 32.94 | 0.047 | 33.30 | 0.051 |
| ComGS-l (ours) | 28.76 | 0.154 | 33.26 | 0.094 | 33.53 | 0.104 |
| Method | Flame Salmon | | Flame Steak | | Sear Steak | |
| | PSNR (dB \uparrow) | Storage (MB \downarrow) | PSNR (dB \uparrow) | Storage (MB \downarrow) | PSNR (dB \uparrow) | Storage (MB \downarrow) |
| KPlanes [17] | 30.44 | 1.0 | 32.38 | 1.0 | 32.52 | 1.0 |
| NeRFPlayer [29] | 31.65 | 18.4 | 31.93 | 18.4 | 29.12 | 18.4 |
| HyperReel [30] | 28.26 | 1.2 | 32.20 | 1.2 | 32.57 | 1.2 |
| 4DGS [19] | 29.38 | 29.0 | 34.03 | 29.0 | 33.51 | 29.0 |
| 4D-GS [11] | 29.20 | 0.3 | 32.51 | 0.3 | 32.49 | 0.3 |
| Spacetime-GS [12] | 29.48 | 0.7 | 33.40 | 0.7 | 33.46 | 0.7 |
| E-D3DGS [39] | 29.72 | 0.5 | 33.55 | 0.5 | 33.55 | 0.5 |
| StreamRF [25] | 28.26 | 31.84 | 32.24 | 31.84 | 32.36 | 31.84 |
| 3DGStream [13] | 28.42 | 7.80 | 34.30 | 7.80 | 33.01 | 7.80 |
| QUEEN-I [32] | 29.25 | 1.00 | 34.17 | 0.59 | 33.93 | 0.56 |
| ComGS-s (ours) | 29.31 | 0.052 | 33.42 | 0.045 | 33.59 | 0.040 |
| ComGS-l (ours) | 29.58 | 0.129 | 33.84 | 0.083 | 33.74 | 0.0704 |

Table 9: **Per-scene quantitative results on the MeetRoom dataset.**

| Method | Discussion | Stepin | Trimming | VrHeadset |
|----------------------------|------------|--------|----------|-----------|
| PSNR (dB \uparrow) | 31.72 | 30.17 | 32.12 | 31.95 |
| Storage (KB \downarrow) | 37.5 | 24.2 | 27.0 | 24.5 |

C Limitations and Future Works

Despite achieving significant improvements, there are several limitations that constrains the performance of our ComGS, which would be addressed in future works. First, as the first frame serves as the foundation for subsequent frame updates, poor initialization would lead to error propagation and degraded performance. Developing a robust and efficient initialized strategy for first frame could further improve the visual quality and storage efficiency of online FVV. Second, while this paper mainly focuses on designing a compact representation for online FVV, it does not fully consider the training time of the encoding stage, leaving room for further improvements in training efficiency. Additionally, our method relies on the dense view videos as inputs, which is expensive for practical applications. Future work will explore extending the framework to sparse-view or monocular inputs for real-world scenarios.

D Broader Impact

Our work is a positive technology. This method reconstructs free-viewpoint videos from multi-view 2D videos in a streaming manner, which can improve the immersive and interactive experience of

viewers. As discussed in the introduction, this technology has potential to benefit various aspects of daily life, including applications in remote diagnosis and 3D video conferencing.

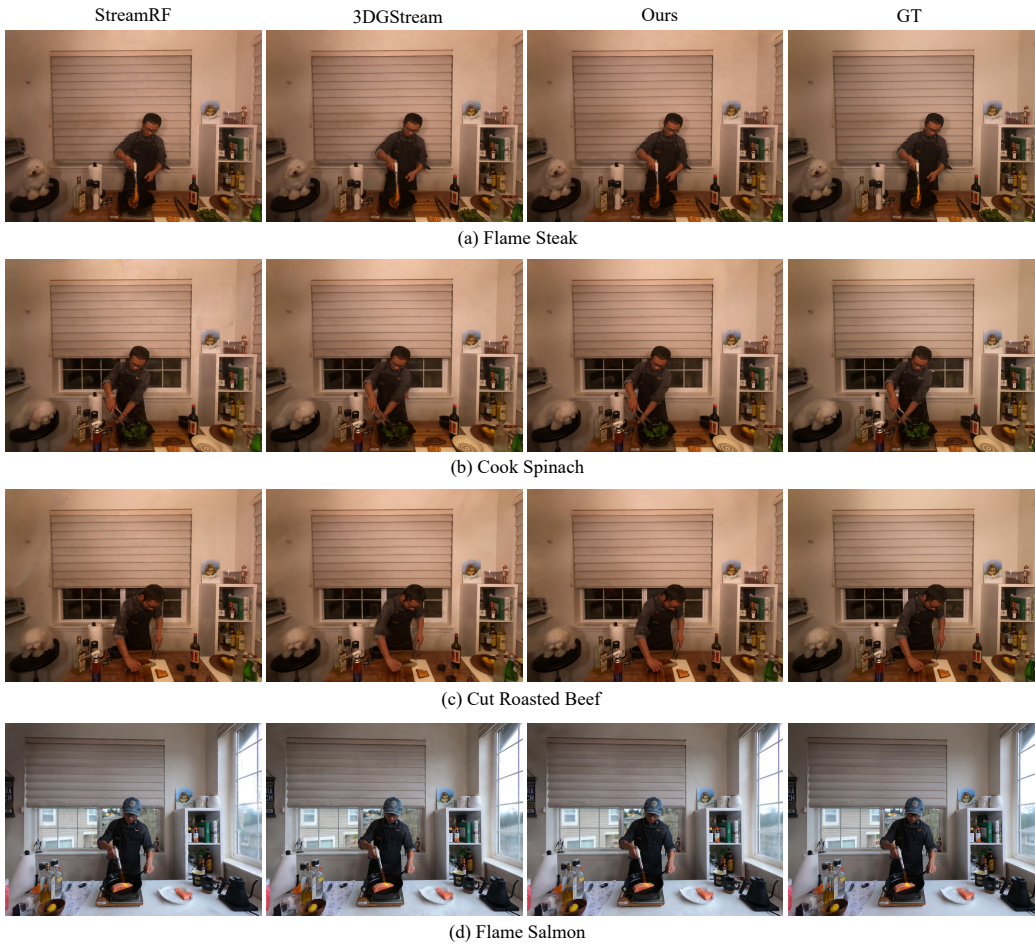


Figure 8: Comparison on N3DV [14] dataset.

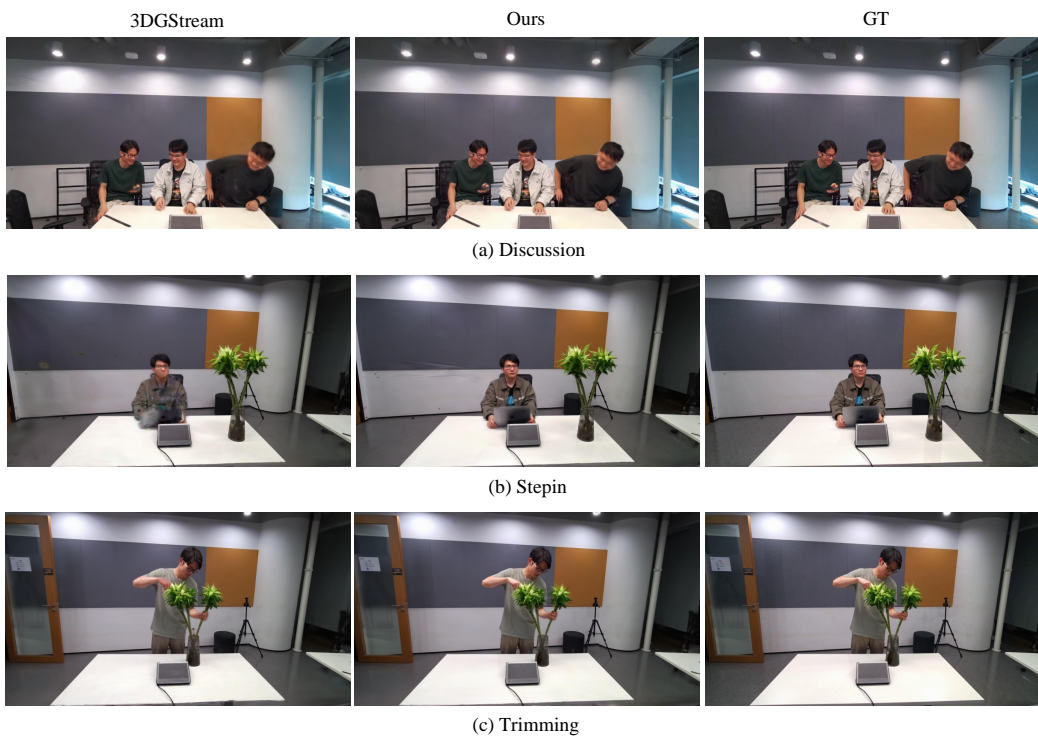


Figure 9: Comparison on MeetRoom [25] dataset.